Article

# Nanocrystalline Iron Oxide Aerogels as Mesoporous Magnetic Architectures

Jeffrey W. Long, Michael S. Logan, Christopher P. Rhodes,
Everett E. Carpenter, Rhonda M. Stroud, and Debra R. Rolison

*J. Am. Chem. Soc.*, **2004**, 126 (51), 16879-16889• DOI: 10.1021/ja046044f • Publication Date (Web): 04 December 2004



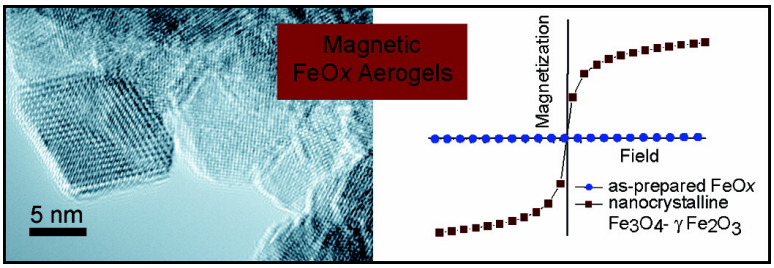


## More About This Article

Additional resources and features associated with this article are available within the HTML version:

- Supporting Information
- Links to the 12 articles that cite this article, as of the time of this article download
- Access to high resolution figures
- Links to articles and content related to this article
- Copyright permission to reproduce figures and/or text from this article

View the Full Text HTML

J|A|C|S
ARTICLES
Published on Web 12/04/2004

# Nanocrystalline Iron Oxide Aerogels as Mesoporous Magnetic Architectures

Jeffrey W. Long,*,† Michael S. Logan,† Christopher P. Rhodes,†
Everett E. Carpenter,‡,§ Rhonda M. Stroud,‡ and Debra R. Rolison*,†

*Contribution from the Surface Chemistry (Code 6170) and Materials and Sensors (Code 6360) Branches, Naval Research Laboratory, Washington, D.C. 20375*

Received July 2, 2004; E-mail: jwlong@ccs.nrl.navy.mil; rolison@nrl.navy.mil

***Abstract:*** We have developed crystalline nanoarchitectures of iron oxide that exhibit superparamagnetic behavior while still retaining the desirable bicontinuous pore−solid networks and monolithic nature of an aerogel. Iron oxide aerogels are initially produced in an X-ray-amorphous, high-surface-area form, by adapting recently established sol−gel methods using Fe(III) salts and epoxide-based proton scavengers. Controlled temperature/atmosphere treatments convert the as-prepared iron oxide aerogels into nanocrystalline forms with the inverse spinel structure. As a function of the bathing gas, treatment temperature, and treatment history, these nanocrystalline forms can be reversibly tuned to predominantly exhibit either $Fe_3O_4$ (magnetite) or $\gamma$-$Fe_2O_3$ (maghemite) phases, as verified by electron microscopy, X-ray and electron diffraction, microprobe Raman spectroscopy, and magnetic analysis. Peak deconvolution of the Raman-active Fe−O bands yields valuable information on the local structure and vacancy content of the various aerogel forms, and facilitates the differentiation of $Fe_3O_4$ and $\gamma$-$Fe_2O_3$ components, which are difficult to assign using only diffraction methods. These nanocrystalline, magnetic forms retain the inherent characteristics of aerogels, including high surface area (>140 $m^2$ $g^{-1}$), through-connected porosity concentrated in the mesopore size range (2−50 nm), and nanoscale particle sizes (7−18 nm). On the basis of this synthetic and processing protocol, we produce multifunctional nanostructured materials with effective control of the pore−solid architecture, the nanocrystalline phase, and subsequent magnetic properties.

## Introduction

Iron oxides are a versatile class of materials that enable a wide range of technologies, many of which are contingent on the distinct magnetic properties of iron oxide (FeO*x*) and related mixed-metal ferrites.[1] The magnetic behavior of nano-FeO*x* is exploited for magnetic recording[2] and various biomedical applications,[3,4] including separations, imaging, and drug delivery. The reactivity and amplified surface areas of nanoscale iron oxides are used in designing substrates for heterogeneous catalysis, both as stand-alone catalysts[5,6] and in composites with precious metals such as Au.[7,8] Iron oxide phases that exhibit mixed ion−electron conductivity are also being investigated as active electrode materials for lithium batteries[9−13] and electrochemical capacitors,[14] where nanoscale forms of iron oxide exhibit improved electrochemical capacity and reversibility.

Many of these technologically important uses of nanoscale iron oxide require facile molecular flux to achieve high performance. We have shown for a wide range of rate-critical applications that creating pore−solid nanoarchitectures with through-connected porosity can improve performance per unit time by factors of >100 relative to materials with interrupted porosity.[15−18] Distributing an active material in a three-dimensional (3-D) nanoarchitecture further serves to immobilize and stabilize the active nanophase material as well as spatially distribute the nanoparticles for interaction with liquid- or gas-phase species. Aerogel nanoarchitectures prepared by sol−gel chemistry and

† Surface Chemistry Branch (Code 6170).
‡ Materials and Sensors Branch (Code 6360).
§ Present address: Department of Chemistry, Virginia Commonwealth University, Richmond, VA 23284.

(1) Kodama, R. H. *J. Magn. Magn. Mater.* **1999**, *200*, 359−372.
(2) Pankhurst, Q. A.; Pollard, R. J. *J. Phys.: Condens. Matter* **1993**, *5*, 8487−8508.
(3) Pankhurst, Q. A.; Connolly, J.; Jones, S. K.; Dobson, J. *J. Phys. D: Appl. Phys.* **2003**, *36*, R167−R181.
(4) Shinkai, M. *J. Biosci. Bioeng.* **2002**, *94*, 606−613.
(5) Li, P.; Miser, D. E.; Rabiei, S.; Yadav, R. T.; Hajaligol, M. R. *Appl. Catal. B−Environ.* **2003**, *43*, 151−162.
(6) Mahajan, D.; Gutlich, P.; Stumm, U. *Catal. Commun.* **2003**, *4*, 101−107.
(7) Andreeva, D.; Tabakova, T.; Idakiev, V.; Christov, P.; Giovanoli, R. *Appl. Catal. A: Gen.* **1998**, *169*, 9−14.
(8) Hua, J. M.; Wei, K. M.; Zheng, Q.; Lin, X. Y. *Appl. Catal. A: Gen.* **2004**, *259*, 121−130.
(9) Jain, G.; Capozzi, C. J.; Xu, J. J. *J. Electrochem. Soc.* **2003**, *150*, A806−A810.
(10) Lee, Y. S.; Sato, S.; Sun, Y. K.; Kobayakawa, K.; Sato, Y. *J. Power Sources* **2003**, *119*, 285−289.
(11) Prosini, P. P.; Carewska, M.; Loreti, S.; Minarini, C.; Passerini, S. *Int. J. Inorg. Mater.* **2000**, *2*, 365−370.
(12) Sarradin, J.; Ribes, M.; Guessous, A.; Elkacemi, K. *Solid State Ionics* **1998**, *112*, 35−40.
(13) Xu, J. J.; Jain, G. *Electrochem. Solid-State Lett.* **2003**, *6*, A190−A193.
(14) Wu, N. L.; Wang, S. Y.; Han, C. Y.; Wu, D. S.; Shiue, L. R. *J. Power Sources* **2003**, *113*, 173−178.
(15) Leventis, N.; Elder, I.; Rolison, D. R.; Anderson, M. L.; Merzbacher, C. I. *Chem. Mater.* **1999**, *11*, 2837−2845.
(16) Anderson, M. L.; Stroud, R. M.; Rolison, D. R. *Nano Lett.* **2002**, *2*, 235−240; *Nano Lett.* **2003**, *3*, 1321 (correction).
(17) Wallace, J. M.; Rice, J. K.; Pietron, J. J.; Stroud, R. M.; Long, J. W.; Rolison, D. R. *Nano Lett.* **2003**, *3*, 1463−1467.
(18) Rolison, D. R. *Science* **2003**, *299*, 1698−1701.

supercritical fluid processing combine intrinsic properties of nanoscale pore and solid that make them attractive candidates for a variety of applications that rely on the flux of molecules or ions to and from active surfaces: a bonded, self-wired nanoscale solid network and a through-connected, 3-D aperiodic network of porosity, with pores typically in the mesopore size range (2−50 nm).[19−22]

Nanoscale iron oxides have been produced in mesoporous forms using surfactant templating[23−25] and have also been incorporated into various preformed porous matrices, including templated, mesoporous silicates and aluminosilicates,[26−31] nanochannel alumina,[32] silica xerogels,[33−46] and silica aerogels.[47−53] When the FeO*x* component of the composite aerogels is produced in certain nanocrystalline phases, the resulting aerogels exhibit soft magnetic behavior[47,48] and are potentially useful as magneto-optical sensors. Free-standing FeO*x* aerogels have also been reported and investigated for catalytic applications.[54] Gash et al. recently developed a highly versatile sol−gel technique for the synthesis of oxide aerogels, based on the reaction of trivalent or tetravalent metal salts with various epoxide-based proton scavengers.[55−57] Using an Fe(III) precursor, FeO*x* aerogels were generated in either noncrystalline forms or as $\beta$-FeOOH (akaganeite), which could be further calcined at 515 °C to form crystalline $\alpha$-$Fe_2O_3$ (hematite) aerogels.[56,57]

We now report an adaptation of the epoxide-based synthetic approach with the specific goal of achieving crystalline, magnetic FeO*x* aerogel nanoarchitectures, rather than forming nanoparticles or guests in other oxide hosts. Magnetic FeO*x* spinel phases, with characteristics of $Fe_3O_4$ (magnetite) and $\gamma$-$Fe_2O_3$ (maghemite), are produced by processing the as-prepared, X-ray-amorphous FeO*x* aerogels under controlled temperature/atmosphere conditions. Although moderately densified relative to the as-prepared form, these magnetic, nanocrystalline forms of FeO*x* retain the desirable physical properties of an aerogel: high surface area, through-connected porosity in the mesopore and small macropore size range (10−80 nm), and nanoscale particle sizes (7−18 nm). These synthetic and processing protocols also provide for sufficient control to tune the pore−solid architecture, FeO*x* nanocrystalline phase, and resulting magnetic properties.

## Experimental Section

**Synthesis and Processing Methods for FeO*x* Aerogels.** Iron oxide aerogels are prepared by minor modification of a previously reported procedure using epoxide-based proton scavengers to initiate the sol−gel reactions of hydrolysis and polycondensation.[55,56] Various epoxides promote the hydrolysis of Fe(III) salts; for our study, we chose epichlorohydrin because of its greater chemical stability relative to propylene oxide. The typical synthesis begins by preparing 0.35 M $FeCl_3 \cdot 6H_2O$ (Alfa Aesar) in anhydrous ethanol (Warner-Graham). To this solution, epichlorohydrin (Aldrich) was added dropwise with stirring (10:1 molar ratio of epoxide:Fe). After ∼5 min of stirring, the FeO*x* sol was transferred into several cylindrical high-density polyethylene molds (Zinsser), which were sealed with plastic wrap. Gelation occurred after ∼1 h, after which the gels were aged for another 16 h. The gels were then transferred to beakers in which a series of solvent exchanges was performed over several days, starting with anhydrous ethanol and proceeding to acetone (Fisher Scientific). All reagents were used as received.

The acetone-filled gels were transferred under acetone into a critical-point dryer (Polaron Range, Quorum Technologies, New Haven, East Sussex, UK) maintained at 10 °C, and the autoclave was then filled with liquid $CO_2$. After a series of pore−fluid exchanges with liquid $CO_2$ over 6 h, the temperature within the autoclave was increased beyond the critical point of $CO_2$ ($T_c$ = 31 °C; $P_c$ = 7.4 MPa). Supercritical $CO_2$ was slowly vented from the autoclave, resulting in dry iron oxide aerogels that retained the dimensions of the wet gel.

The aerogels were heat-treated in a fused quartz tube in a Lindberg programmable tube furnace by ramping at 2 °C $min^{-1}$, holding at the predetermined temperature for 20 h, and then cooling to ambient temperature at 2 °C $min^{-1}$. Thermal treatments were performed in either static ambient air or flowing argon at 56 cm $min^{-1}$. The various samples are denoted according to their thermal treatments (Table 1).

**Characterization and Instrumentation.** Surface areas and porosities were determined by nitrogen physisorption using a Micromeritics

(19) Fricke, J.; Emmerling, A. *J. Sol-Gel Sci. Technol.* **1998**, *13*, 299−303.
(20) Hüsing, N.; Schubert, U. *Angew. Chem., Int. Ed.* **1998**, *37*, 23−45.
(21) Pierre, A. C.; Pajonk, G. M. *Chem. Rev.* **2002**, *102*, 4243−4265.
(22) Rolison, D. R.; Dunn, B. *J. Mater. Chem.* **2001**, *11*, 963−980.
(23) Lezau, A.; Trudeau, M.; Tsoi, G. M.; Wenger, L. E.; Antonelli, D. *J. Phys. Chem. B* **2004**, *108*, 5211−5216.
(24) Yuan, Z. Y.; Ren, T. Z.; Su, B. L. *Catal. Today* **2004**, *93*−*95*, 743−750.
(25) Srivastava, D. N.; Perkas, N.; Gedanken, A.; Felner, I. *J. Phys. Chem. B* **2002**, *106*, 1878−1883.
(26) Wong, S. T.; Lee, J. F.; Cheng, S. F.; Mou, C. Y. *Appl. Catal. A: Gen.* **2000**, *198*, 115−126.
(27) Selvam, P.; Dapurkar, S. E.; Badamali, S. K.; Murugasan, M.; Kuwano, H. *Catal. Today* **2001**, *68*, 69−74.
(28) Dapurkar, S. E.; Badamali, S. K.; Selvam, P. *Catal. Today* **2001**, *68*, 63−68.
(29) Zhang, L.; Papaefthymiou, G. C.; Ying, J. Y. *J. Phys. Chem. B* **2001**, *105*, 7414−7423.
(30) Garcia, C.; Zhang, Y. M.; DiSalvo, F.; Wiesner, U. *Angew. Chem., Int. Ed.* **2003**, *42*, 1526−1530.
(31) Samanta, S.; Giri, S.; Sastry, P. U.; Mal, N. K.; Manna, A.; Bhaumik, A. *Ind. Eng. Chem. Res.* **2003**, *42*, 3012−3018.
(32) Tofail, S. A. M.; Rahman, I. Z.; Rahman, M. A.; Sutton, D.; Newcomb, S. B. *J. Magn. Magn. Mater.* **2002**, *242*, 588−590.
(33) Caizer, C.; Savii, C.; Popovici, M. *Mater. Sci. Eng. B−Solid State Mater. Adv. Technol.* **2003**, *97*, 129−134.
(34) Savii, C.; Popovici, M.; Enache, C.; Subrt, J.; Niznansky, D.; Bakardzieva, S.; Caizer, C.; Hrianca, I. *Solid State Ionics* **2002**, *151*, 219−227.
(35) Das, D.; Roy, S.; Chen, J. W.; Chakravorty, D. *J. Appl. Phys.* **2002**, *91*, 4573−4579.
(36) Cannas, C.; Concas, G.; Falqui, A.; Musinu, A.; Spano, G.; Piccaluga, G. *J. Non-Cryst. Solids* **2001**, *286*, 64−73.
(37) Cannas, C.; Concas, G.; Gatteschi, D.; Falqui, A.; Musinu, A.; Piccaluga, G.; Sangregorio, C.; Spano, G. *Phys. Chem. Phys.* **2001**, *3*, 832−838.
(38) Yasumori, A.; Matsumoto, H.; Hayashi, S.; Okada, K. *J. Sol-Gel Sci. Technol.* **2000**, *18*, 249−258.
(39) Iijima, S.; Nomura, A.; Mizukami, F.; Shin, S.; Mizutani, F. *J. Radioanal. Nucl. Chem.* **1999**, *239*, 297−302.
(40) Shen, J. C.; Ebner, A. D.; Ritter, J. A. *J. Colloid Interface Sci.* **1999**, *214*, 333−343.
(41) Ennas, G.; Casula, M. F.; Piccaluga, G.; Solinas, S.; Morales, M. P.; Serna, C. J. *J. Mater. Res.* **2002**, *17*, 590−596.
(42) Zaharescu, M.; Crisan, M.; Jitianu, A.; Crisan, D.; Meghea, A.; Rau, I. *J. Sol-Gel Sci. Technol.* **2000**, *19*, 631−635.
(43) Peleanu, I.; Zaharescu, M.; Rau, I.; Crisan, M.; Jitianu, A.; Meghea, A. *J. Radioanal. Nucl. Chem.* **2000**, *246*, 557−563.
(44) Niznansky, D.; Viart, N.; Rehspringer, J. L. *J. Sol-Gel Sci. Technol.* **1997**, *8*, 615−618.
(45) Ponce-Castañeda, S.; Martínez, J. R.; Ruiz, F.; Palomares-Sánchez, S.; Dominguez, O.; Ruiz, F.; Matutes-Aquino, J. A. *J. Sol-Gel Sci. Technol.* **2002**, *25*, 29−36.
(46) Moreno, E. M.; Zayat, M.; Morales, M. P.; Serna, C. J.; Roig, A.; Levy, D. *Langmuir* **2002**, *18*, 4972−4978.
(47) Cannas, C.; Casula, M. F.; Concas, G.; Corrias, A.; Gatteschi, D.; Falqui, A.; Musinu, A.; Sangregorio, C.; Spano, G. *J. Mater. Chem.* **2001**, *11*, 3180−3187.
(48) Casas, L.; Roig, A.; Rodríguez, E.; Molins, E.; Tejada, J.; Sort, J. *J. Non-Cryst. Solids* **2001**, *285*, 37−43.
(49) Wang, C. T.; Willey, R. J. *J. Catal.* **2001**, *202*, 211−219.
(50) Fabrizioli, P.; Bürgi, T.; Burgener, M.; van Doorslaer, S.; Baiker, A. *J. Mater. Chem.* **2002**, *12*, 619−630.
(51) Fabrizioli, P.; Bürgi, T.; Baiker, A. *J. Catal.* **2002**, *206*, 143−154.
(52) Casas, L.; Roig, A.; Molins, E.; Grenèche, J. M.; Asenjo, J.; Tejada, J. *Appl. Phys. A−Mater. Sci. Processing* **2002**, *74*, 591−597.
(53) Casula, M. F.; Corrias, A.; Paschina, G. *J. Non-Cryst. Solids* **2001**, *293*, 25−31.
(54) Wang, C. T.; Willey, R. J. *Catal. Today* **1999**, *52*, 83−89.
(55) Gash, A. E.; Tillotson, T. M.; Satcher, J. H.; Hrubesh, L. W.; Simpson, R. L. *J. Non-Cryst. Solids* **2001**, *285*, 22−28.
(56) Gash, A. E.; Tillotson, T. M.; Satcher, J. H.; Poco, J. F.; Hrubesh, L. W.; Simpson, R. L. *Chem. Mater.* **2001**, *13*, 999−1007.
(57) Gash, A. E.; Satcher, J. H.; Simpson, R. L. *Chem. Mater.* **2003**, *15*, 3268−3275.

***Table 1.*** Physical Properties of FeO*x* Aerogels as a Function of Thermal Treatment

| sample notation | treatment[a] | surface area ($m^2\ g^{-1}$)[b] | cumulative pore volume ($cm^3\ g^{-1}$)[c] | mean pore diameter (nm)[c] | particle size (nm) | | saturation magnetization (emu $g^{-1}$)[e] | blocking temperature (K) |
|---|---|---|---|---|---|---|---|---|
| | | | | | $XRD_{311}$[d] | TEM | | |
| as-prepared | as-prepared | 464 | 4.06 | 31 | na | na | no saturation | 15 |
| 260-AIR | 260 °C in air | 240 | 2.58 | 33 | 5 | 4 | no saturation | 50 |
| 320-AIR | 320 °C in air | 160 | 1.74 | 35 | 11 | −[f] | 7.7 | 70 |
| 260-ARG | 260 °C in argon | 143 | 1.04 | 29 | 9 | 7 | 44.4 | 170 |
| 320-ARG | 320 °C in argon | 77.0 | 0.450 | 17 | 14 | − | − | rt |
| 370-ARG | 370 °C in argon | 54.8 | 0.426 | 30 | 27 | 18.5 | 57.4 | rt |
| 260-ARG-AIR | 260 °C in argon, 260 °C in air | 132 | 0.946 | 29 | 7 | 8.5 | 26.0 | 68 |
| 260-ARG-AIR-ARG | 260 °C in argon, 260 °C in air, 260 °C in argon | 138 | 0.962 | 30 | 12 | 8.5 | 41.0 | 140 |

[a] Samples are heated at the designated temperatures for 20 h, with a temperature ramp of 2 °C $min^{-1}$ on both heating and cooling cycles. [b] Multipoint BET method; replicate analyses are ±5%. [c] BJH method, adsorption isotherm, representing the volume in pores between 1.7 and 300 nm. [d] Scherrer analysis of the (311) diffraction peak. [e] Measured at room temperature. [f] −, not measured.

ASAP2010 accelerated surface area and porosimetry analyzer. All samples were degassed at 80 °C for at least 24 h prior to characterization, except for the as-prepared aerogel, which was degassed at 50 °C for at least 48 h. Higher degassing temperatures were avoided as we observed some evidence for densification and/or deoxygenation of FeO*x* aerogels under more extreme temperature/vacuum conditions. Pore-size distributions were calculated from adsorption isotherm data using Micromeritics DFTPlus software (Halsey thickness model, cylindrical pore). Thermal analysis was performed using a Rheometrics STA1500 simultaneous thermal analyzer, which records both thermogravimetric analysis (TGA) and differential scanning calorimetry (DSC) in a single measurement. A Micromeritics Ultramicro He pycnometer was used to determine the skeletal density of the highly porous iron oxides. The envelope densities of FeO*x* monoliths were determined using Hg-displacement measurements in a specific gravity bottle. X-ray diffraction was performed on ground powders of the FeO*x* aerogels using a Bruker D8 Advance X-ray diffractometer. Scans were recorded for $2\theta$ values between 20 and 70°, using a step size of 0.02° and integration of 16 s per step. For crystalline samples, the particle sizes were calculated from the $XRD_{311}$ peak width using the Scherrer equation.

Transmission electron microscopy was used to characterize the aerogel morphologies and to confirm particle size and crystal structure. Samples were prepared by dry-grinding the aerogel powders and then brushing the dust onto holey-carbon film supports.[58,59] The data were obtained using a JEOL 2010F TEM equipped with a Gatan CCD camera and Noran Vantage EDS.

The Raman spectra were obtained with a Renishaw RM1000 Raman spectrometer using a backscattering geometry. The 514-nm line of an argon-ion laser was focused through an Olympus microscope with a 50× lens to give a spot size of ~1 $\mu$m. Spectra were obtained using a 16-s acquisition time and averaged over 10 accumulations. The laser power was controlled using a series of optical density filters and kept below ~1 mW to avoid sample degradation. Laser-induced thermal effects were observed in previous Raman studies of iron oxides, and low laser powers are necessary to minimize spectral changes due to local heating.[60,61] To verify that the laser did not induce spectral changes, spectra were obtained at a laser power of 0.1 mW and the same acquisition and sampling conditions as above; no differences were observed compared to the spectra taken at 1 mW. The spectra of polycrystalline magnetite (Aldrich, 99.99%) and maghemite (Aldrich, 99.9%) were obtained to compare to the aerogel samples. Visual inspection of the aerogel samples, post-analysis, using white light illumination did not reveal any laser-induced changes. The data were analyzed and curve-fit using Grams version 5.2 (Galactic, Inc.) spectral analysis software. Spectra were curve-fit to a straight baseline with one Gaussian−Lorentian product function for each band using a nonlinear least-squares algorithm.

Powdered materials were weighed out and placed in a gelatin capsule for magnetic characterization[62,63] by vibrating sample magnetometry (VSM; LakeShore vibrating sample magnetometer) and thermal magnetization (Quantum Design MPMS-5S SQUID magnetometer). The powder-filled capsule was placed into a polystyrene straw and attached to the sample arm of the VSM. Magnetization vs field curves were collected from −10 to 10 kOe. Magnetization vs temperature curves were collected from 5 to 300 K at two field strengths (50 and 2000 Oe) to assess the superparamagnetic behavior of the porous iron oxide nanoarchitectures.

## Results and Discussion

**Characterization of As-Prepared FeO*x* Aerogels.** Reacting iron(III) salts with epichlorohydrin as the proton scavenger yields monolithic orange-red gels. Supercritical $CO_2$ extraction of the wet gels renders the low-density, monolithic aerogel form. The as-prepared aerogels exhibit high surface area (464 $m^2\ g^{-1}$) and substantial pore volume (4.0 $cm^3\ g^{-1}$) (Table 1), consistent with the initial reports of propylene-oxide-derived FeO*x* aerogels.[56] The data obtained by $N_2$ porosimetry can also be used to derive pore-size distribution (PSD) plots using fitting routines with one of several available models.[64,65] The generation of PSD plots is particularly important for an accurate description of aerogels, which exhibit aperiodic pore−solid architectures. The pore volume for the as-prepared FeO*x* aerogel is distributed over a wide range of pore sizes, from 2 to 140 nm (see Figure 1a), with no significant microporosity (pores < 2 nm). A large fraction of the pore volume is macroporous, centered in ~80-nm pores.

The as-prepared FeO*x* aerogels exhibit thermogravimetric transitions (Figure 2) that are likely due to the loss of physisorbed and structural water, as well as organic byproducts of the initial synthesis.[57,66] The as-prepared aerogel loses ~25%

(58) Previous small-angle neutron scattering and porosimetry measurements with silica aerogels confirm that the pore−solid architecture of an aerogel powder reflects that of the monolith from which it was derived.[59]

(59) Merzbacher, C. I.; Barker, J. G.; Swider, K. E.; Rolison, D. R. *J. Non-Cryst. Solids* **1998**, *224*, 92−96.
(60) Bersani, D.; Lottici, P. P.; Montenero, A. *J. Raman Spectrosc.* **1999**, *30*, 355−360.
(61) de Faria, D. L. A.; Silva, S. V.; de Oliveira, M. T. *J. Raman Spectrosc.* **1997**, *28*, 873−878.
(62) O'Connor, C. J. *Prog. Inorg. Chem.* **1982**, *29*, 202.
(63) O'Connor, C. J. *Research Frontiers in Magnetochemistry*; World Scientific: River Edge, NJ, 1993.
(64) Sonwane, C. G.; Bhatia, S. K. *J. Phys. Chem. B* **2000**, *104*, 9099−9110.
(65) Kaneko, K. *J. Membr. Sci.* **1994**, *96*, 59−89.

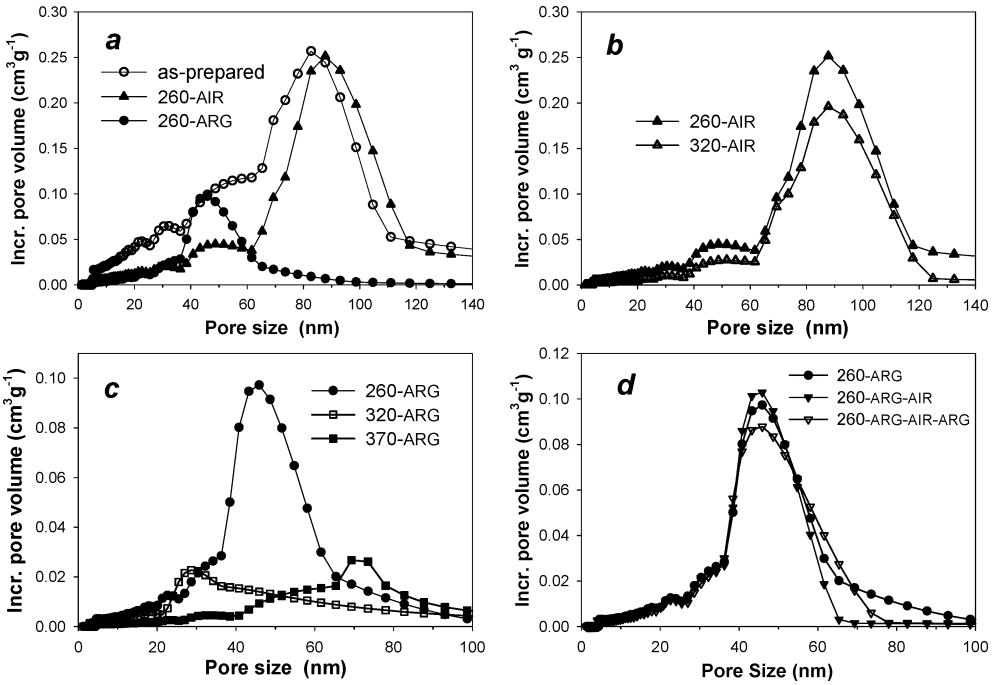


***Figure 1.*** Pore-size distribution plots for various FeO*x* aerogel samples. These plots are generated using a Halsey thickness model fitting (cylindrical pore) of the experimental $N_2$ adsorption data.

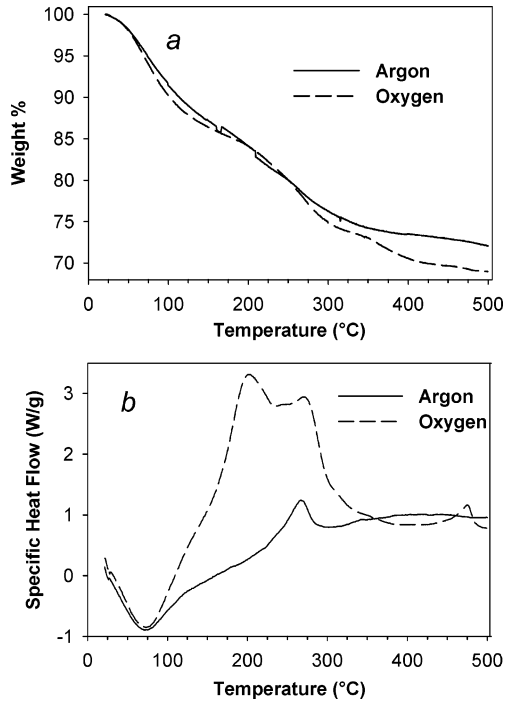


***Figure 2.*** Simultaneous thermal analysis for the as-prepared FeO*x* aerogel in either flowing argon or oxygen: (a) thermogravimetric analysis and (b) differential scanning calorimetry. Measurements are performed with a 2 °C $min^{-1}$ heating ramp.

of its initial mass in two broad features over temperatures from ambient to 320 °C, whether the atmosphere is flowing oxygen or argon. The loss of physisorbed water at temperatures less than 100 °C is confirmed in the simultaneous DSC measurements (Figure 2b), where nearly identical endothermic peaks are observed in both gas flows. In a separate series of experiments, X-ray photoelectron spectroscopy (XPS) was used to quantify the elemental compositions of representative FeO*x* aerogels subjected to different thermal treatments (see Supporting Information). Those measurements confirmed that carbon (in the form of oxygenated species) is lost when as-prepared FeO*x* aerogels are heated at 320 °C, and the final carbon content of the heated samples is the same regardless of the bathing gas (argon vs air).

Under inert argon flow conditions, the as-prepared aerogels exhibit a single exotherm at ∼265 °C (specific heat ∼260 J $g^{-1}$), possibly due to a crystallization. A similar peak is observed under oxygen flow, but with the addition of a much larger exothermic peak at ∼200 °C, and these two combined exothermic features yield a specific heat of ∼3400 J $g^{-1}$. The source of this additional exothermic peak is presently unknown, but may be due to reactions of residual chlorine/chloride contamination from the initial reagents, either $FeCl_3 \cdot 6H_2O$, epichlorohydrin, or their byproducts. Elemental analysis by XPS demonstrated that the relative chlorine content (Cl:Fe) of FeO*x* aerogels heated at 320 °C in air decreased by 50%, whereas aerogels heated in argon retained the same relative chlorine content as the initial as-prepared aerogel (see Supporting Information). A smaller exotherm occurs in the DSC trace at ∼460 °C, presumably indicating a further phase transition only under oxygen flow. In the present report, we limit the thermal treatments to temperatures at or below 370 °C.

**Thermal Processing of FeO*x* Aerogels.** Iron oxide aerogels heated directly in air darken from orange-red to red-brown and densify, but the 260-AIR aerogel retains very high surface area (240 $m^2$ $g^{-1}$) and pore volume (2.58 $cm^3$ $g^{-1}$). The loss of pore volume relative to the as-prepared aerogel is nonspecific for pore sizes between 2 and 60 nm, while the larger pores are preserved, as indicated in Figure 1a. Aerogels calcined at 320 °C exhibit some further decrease in surface area and pore volume but retain a pore-size distribution very similar to that for the 260-AIR aerogel (Table 1).

(66) Dong, W. T.; Zhu, C. S. *J. Mater. Chem.* **2002**, *12*, 1676−1683.

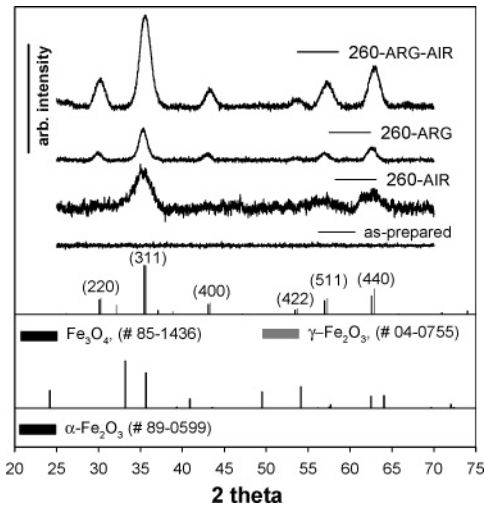


***Figure 3.*** Powder X-ray diffraction patterns for various FeO*x* aerogels, presented after background subtraction. Also shown are JCPDS patterns for $Fe_3O_4$ (no. 85-1436), $\gamma$-$Fe_2O_3$ (no. 04-0755), and $\alpha$-$Fe_2O_3$ (no. 89-0599).

When as-prepared FeO*x* aerogels are thermally processed in an argon atmosphere, they undergo more densification than do the calcined samples, and they exhibit a blue-black color, normally indicative of the $Fe_3O_4$ (magnetite) phase. The 260-ARG aerogel displays a greater decrease in surface area (164 $m^2$ $g^{-1}$) and loss of pore volume (1.04 $cm^3$ $g^{-1}$) than does 260-AIR, even though they were treated at the same temperature. As seen in the PSD plot (Figure 1a), this densification from the as-prepared state occurs with the near-complete collapse of pores in the 60−120-nm size range, as well as some pore volume loss in the smaller mesopores. Thermal treatments at higher temperatures in argon progressively lower the surface area and pore volume for samples treated at 320 and 370 °C, and also cause some rearrangement in the pore-size distribution (see Figure 1c).

**Characterization by X-ray Diffraction.** Preliminary attempts to determine the crystalline phase, degree of crystallinity, and primary particle size were performed with X-ray diffraction. The common crystalline phases of iron oxide include two related spinel structures, $\gamma$-$Fe_2O_3$ (maghemite) and $Fe_3O_4$ (magnetite), and a corundum-type structure, $\alpha$-$Fe_2O_3$ (hematite). The as-prepared aerogel is completely amorphous to X-rays, as seen in Figure 3. With treatment to 260 °C in air, two very broad diffraction peaks consistent with either $Fe_3O_4$ or $\gamma$-$Fe_2O_3$ arise. Distinguishing between $Fe_3O_4$ and $\gamma$-$Fe_2O_3$ is difficult because these two phases are structurally similar, as indicated by the JCPDS patterns in Figure 3, and the difficulty is further compounded for nanocrystalline phases where peaks broaden. Iron oxide aerogels treated initially under inert gas flow exhibit a greater degree of crystallinity, with five broad diffraction peaks present for sample 260-ARG. Similar patterns are observed at higher treatment temperatures in argon, with sharpening of the diffraction peaks for samples 320-ARG and 370-ARG, indicating further crystallite growth at these higher temperatures (data not shown). None of the samples studied exhibit any definitive peaks for $\alpha$-$Fe_2O_3$. The formation of hematite is expected at higher processing temperatures, as recently demonstrated by Gash et al. for related FeO*x* aerogels that were calcined at 515 °C.[57]

The diffraction data were also used as a preliminary measure of average particle size, on the basis of a Scherrer analysis of diffraction peak widths for the (311) peak common to magnetite and maghemite. For aerogels treated thermally in air, the particle size ranges from 5 nm for 260-AIR to 11 nm for 320-AIR. Aerogels crystallized under inert conditions have particle sizes ranging from 9 nm for 260-ARG to 27 nm for 370-ARG. As a caveat, the particle sizes calculated from the XRD data may be compromised for samples that contain both $Fe_3O_4$ and $\gamma$-$Fe_2O_3$ phases (or their intermediate forms) and do not account for nonspherical particles or particle-size distributions.

**Transmission Electron Microscopy.** Transmission electron microscopy was used to further examine the crystallinity, particle size, and morphology of the various FeO*x* aerogels. Images of the 260-ARG and 260-AIR samples are compared in Figure 4. The argon treatment clearly results in a larger particle size (~7 nm) with better crystalline order than does the air treatment. The selected-area diffraction pattern for the 260-ARG sample (Figure 4a, inset) indexes to either $Fe_3O_4$ or $\gamma$-$Fe_2O_3$, in agreement with the X-ray diffraction data. The high-resolution image for 260-ARG (Figure 4b) shows some additional lattice spacings that are not apparent in the electron or X-ray diffraction. These 0.4- to 0.8-nm spacings are consistent with a tetragonally distorted form of $\gamma$-$Fe_2O_3$ and indicate that there may be local deviations from the majority cubic phase in some particles. In contrast, the 260-AIR sample is poorly crystalline, exhibiting broad rings in the electron diffraction pattern (Figure 4c) and few discernible fringes in the high-resolution image (Figure 4d).

**Phase Identification with Microprobe Raman Spectroscopy.** Raman spectroscopy is potentially more useful than diffraction techniques in distinguishing $\gamma$-$Fe_2O_3$ and $Fe_3O_4$ and is less reliant on crystallinity for structure identification. Previous studies have shown that the vibrational frequencies of $\gamma$-$Fe_2O_3$ and $Fe_3O_4$ track their subtle structural differences and allow these phases to be differentiated by Raman spectroscopy.[61] The sensitivity of Raman spectroscopy to probe the local environment in these systems is of particular interest as a means to correlate the local structure variations with the overall magnetic behavior of these nanomaterials in a pore−solid architecture.

At room temperature, $Fe_3O_4$ belongs to the inverse spinel cubic structure under the $O_h^7$ ($P4_332$) space group,[67,68] with two nonequivalent Fe positions in the unit cell. The "A" positions (occupied by $Fe^{3+}$) involve tetrahedral coordination around the Fe, and the "B" positions (equally populated by $Fe^{3+}$ and $Fe^{2+}$ ions) have octahedral coordination. Considering the smallest Bravais (unit) cell, there are five Raman active modes ($A_{1g} + E_g + 3T_{2g}$).[69] The 665 $cm^{-1}$ band observed in the Raman spectra of $Fe_3O_4$ (Figure 5) exhibits $A_{1g}$ symmetry and is attributed to vibrational modes consisting of stretching of oxygen atoms along Fe−O bonds in the A positions.[69,70] The existence of a high-frequency shoulder at ~704 $cm^{-1}$ with much smaller relative intensity is also evident.

The structure of $\gamma$-$Fe_2O_3$ is related to the inverse spinel structure of $Fe_3O_4$ but has cation vacancies either distributed randomly throughout the tetrahedral and octahedral sites[71] or located preferentially on the octahedral sites.[72,73] This structure can therefore be represented as $(Fe^{3+})[Fe_{5/3}{}^{3+}\square_{1/3}]O_4$ where

(67) Bragg, W. H. *Philos. Mag.* **1915**, *30*, 305−315.
(68) Fleet, M. E. *Acta Crystallogr. B* **1981**, *37*.
(69) Gasparov, L. V.; Tanner, D. B.; Romero, D. B.; Berger, H.; Margaritondo, G.; Forro, L. *Phys. Rev. B* **2000**, *62*, 7939−7944.
(70) Verble, J. L. *Phys. Rev. B* **1974**, *9*, 5236−5248.
(71) Korobeinikova, A. V.; Fadeeva, V. I.; Reznitskii, L. A. *J. Struct. Chem.* **1976**, *17*, 737−741.

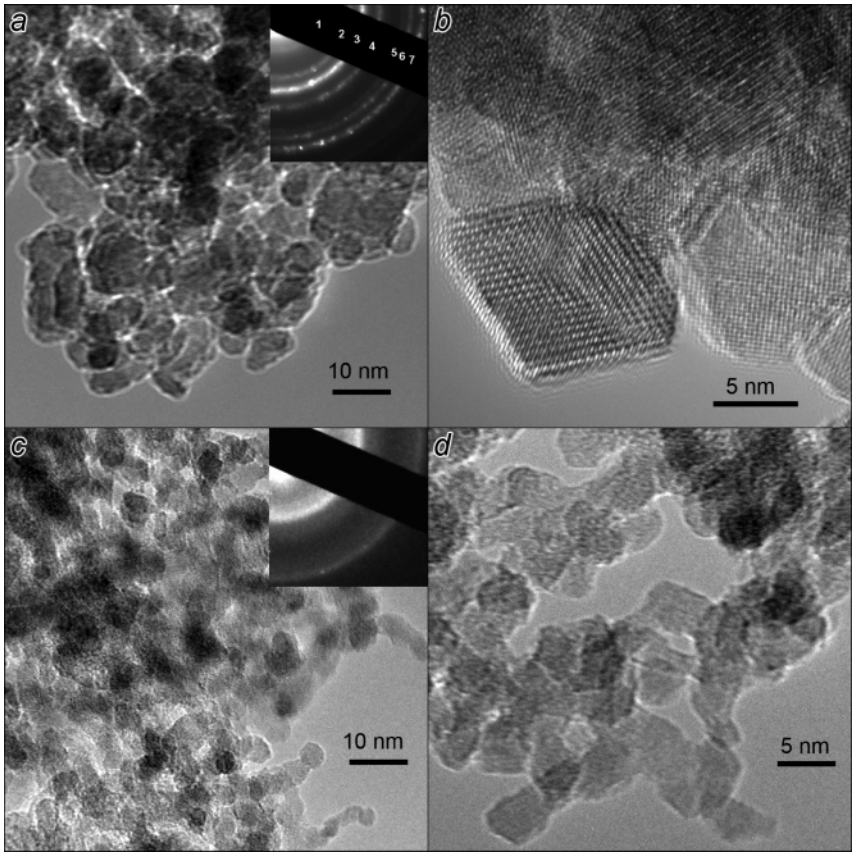


***Figure 4.*** Transmission electron microscopy of the 260-ARG (a,b) and 260-AIR (c,d) samples. The labels on (a) inset correspond to (1) (*111*), (2) (*220*), (3) (*311*), (4) (*400*), (5) (*422*), (6) (*511*), and (7) (*440*) spacings of the $Fe_3O_4$ and $\gamma$-$Fe_2O_3$ spinel-type cubic structures.

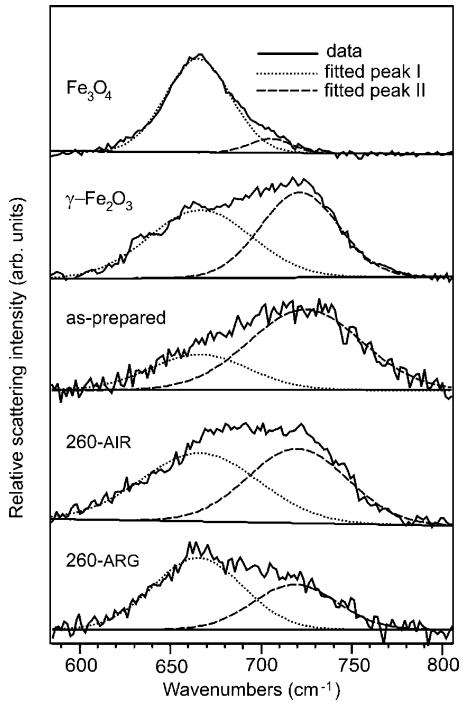


***Figure 5.*** Raman spectra in the 585−805 $cm^{-1}$ region for commercial $\gamma$-$Fe_2O_3$ and $Fe_3O_4$ samples and FeO*x* aerogel samples treated under various temperature/atmosphere conditions. For all samples other than $Fe_3O_4$, the spectra were deconvolved into a band at 665−667 $cm^{-1}$ (peak I) and a band at 720−725 $cm^{-1}$ (peak II) by curve-fitting analysis.

($Fe^{3+}$) refers to tetrahedral coordination, [$Fe_{5/3}$] designates octahedral coordination, and □ denotes a cation vacancy with octahedral coordination.[74] The space group of $\gamma$-$Fe_2O_3$ can be identical to that of $Fe_3O_4$ or symmetry-reduced from cubic ($P4_332$) to tetragonal ($P4_12_12_1$) with vacancy ordering within the structure.[73,75]

Polycrystalline $\gamma$-$Fe_2O_3$ (Figure 5) exhibits Raman bands at 667 and 721 $cm^{-1}$ and additional bands at 505 and 360 $cm^{-1}$ (data not shown), consistent with previous reports.[60,61] The band at 667 $cm^{-1}$ is similar in frequency to the $A_{1g}$ band at 665 $cm^{-1}$ in $Fe_3O_4$ (attributed to in-phase vibrations of $FeO_4$ tetrahedra in the absence of cation vacancies[69,70]), while the band at ~720 $cm^{-1}$ is attributed to vibrational modes of local Fe−O structures in the vicinity of cation vacancies. Cation vacancies in $\gamma$-$Fe_2O_3$ have a strong influence on their local surroundings inducing different Fe−O first neighbor distances for vacancy-poor (2.022Å) and vacancy-rich (2.126Å) cation octahedral positions.[73] The frequency of the $A_{1g}$ mode in $Fe_3O_4$ is also sensitive to local structural displacements, with frequency shifts of >10 $cm^{-1}$.[69]

The synthetic route used to prepare $\gamma$-$Fe_2O_3$ affects the relative population of cation vacancies in the structure[71,74] as well as the relative intensities of the 665 $cm^{-1}$ and 720 $cm^{-1}$ Raman bands. This correlation suggests that the ratio of these two bands may reflect the cation-vacancy content of the $\gamma$-$Fe_2O_3$ structure. We deconvolved our Raman spectra by curve-fitting

(72) Greaves, C. *J. Solid State Chem.* **1983**, *49*, 325−333.
(73) Somogyvari, Z.; Svab, E.; Meszaros, G.; Krezhov, K.; Nedkov, I.; Sajo, I.; Bouree, F. *Appl. Phys. A: Mater.* **2002**, *74*, S1077−S1079.
(74) Belin, T.; Guigue-Millot, N.; Caillot, T.; Aymes, D.; Niepce, J. C. *J. Solid State Chem.* **2002**, *163*, 459−465.
(75) Shmakov, A. N.; Kryukova, G. N.; Tsybulya, S. V.; Chuvilin, A. L.; Solovyeva, L. P. *J. Appl. Crystallogr.* **1995**, *28*, 141−145.

***Table 2.*** Results of Peak-Fitting the Raman Spectra in the 585−805 $cm^{-1}$ Frequency Region for Various FeO*x* Samples (Error in the Relative Areas Is Estimated as ±10%)

| sample | low-frequency band ($cm^{-1}$) | high-frequency band ($cm^{-1}$) | $A_{667}/A_{tot}$[a] | $R^2$ [b] |
|---|---|---|---|---|
| $Fe_3O_4$ | 665 | 704 | 1.00[c] | 0.994 |
| $\gamma$-$Fe_2O_3$ | 667 | 721 | 0.51 | 0.989 |
| as-prepared | 667 | 725 | 0.28 | 0.942 |
| 260-AIR | 667 | 720 | 0.52 | 0.973 |
| 260-ARG | 667 | 724 | 0.73 | 0.943 |
| 260-ARG-AIR | 667 | 720 | 0.49 | 0.956 |
| 260-ARG-AIR-ARG | 667 | 720 | 0.70 | 0.880 |

[a] $A_{667}/A_{tot}$ is defined as the ratio of peak area for the low-frequency band to the total peak area for both fitted peaks. [b] Standard error of peak fits. [c] For the $Fe_3O_4$ sample, the high-frequency band occurred at 704 $cm^{-1}$ (rather than at 720−725 $cm^{-1}$) and had a small area (9%) relative to that of the 667 $cm^{-1}$ band. For this sample, the band intensity at ∼721 $cm^{-1}$ was negligible, and therefore the ratio $A_{667}/A_{tot}$ was considered as 1.00 for $Fe_3O_4$. The origin of the 704 $cm^{-1}$ band is not clear from the present study, and the neglect of the 704 $cm^{-1}$ band in the peak-fitting analysis of the other samples introduces a small error in the relative areas.

with a band between 665 and 667 $cm^{-1}$ and a high-frequency band that was not limited in frequency range, but in all cases occurred between 720 and 725 $cm^{-1}$. The experimental spectra for various iron oxides and the curve-fitted peaks are presented in Figure 5. The relative intensities were determined by dividing the integrated area of the individual peak (e.g., $A_{667}$) by the total integrated area ($A_{tot}$); the results are presented in Table 2.

This deconvolution analysis is valid, provided that additional bands do not significantly contribute to the total Raman intensity in this region and as long as the distribution of local structures is centered around two well-defined environments. This deconvolution analysis is only semiquantitative, however, because the relative areas of the bands may not be directly proportional to the population of cation defects. For example, the scattering cross sections of these modes may differ, and additional factors such as dynamic coupling of modes within a unit cell could influence the frequencies and scattering intensities. A full symmetry-based vibrational analysis is needed to correlate the band frequencies to local structures and determine if the relative peaks areas directly correlate with the population of cation vacancies in $\gamma$-$Fe_2O_3$. With these caveats in mind, the $A_{667}/A_{tot}$ values obtained for polycrystalline $Fe_3O_4$ (1.00) and $\gamma$-$Fe_2O_3$ (0.51) offer a semiquantitative marker for the two phases.

The Raman spectra and fitted peaks for the as-prepared, 260-AIR FeO*x*, and 260-ARG FeO*x* aerogels in the spectral region 600−800 $cm^{-1}$ are shown in Figure 5. The as-prepared aerogel has a broad band centered at 700 $cm^{-1}$, which was fit to peaks at 667 and 725 $cm^{-1}$, although this deconvolution may be problematic due to a broad distribution of local environments. The relative intensity, $A_{667}/A_{tot} = 0.28$, suggests a local structure that is related to $\gamma$-$Fe_2O_3$ ($A_{667}/A_{tot} = 0.51$) but may contain a higher fraction of cation vacancies than the polycrystalline material. Calcination of the as-prepared aerogel in air (sample 260-AIR) alters the local structure, as evidenced by an increase in the relative area of the 667 $cm^{-1}$ band and $A_{667}/A_{tot} = 0.52$, to one highly consistent with the $\gamma$-$Fe_2O_3$ phase. When the as-prepared aerogel is heated in argon (260-ARG), $A_{667}/A_{tot}$ increases to 0.73, which suggests a structure that is intermediate between $Fe_3O_4$ and $\gamma$-$Fe_2O_3$, or the coexistence of distinct $Fe_3O_4$ and $\gamma$-$Fe_2O_3$ phases.

**Summary of FeO*x* Phase Transformations and Their Correlation with Pore−Solid Architecture.** The formation of nanocrystalline FeO*x* aerogels from the initial amorphous form is highly dependent on both the temperature and bathing gas in post-synthesis thermal treatments. Aerogels heated directly in the presence of $O_2$ (from air) are poorly crystalline and are also only moderately densified relative to the as-prepared aerogel. Differences in the Raman spectra of the as-prepared sample and 260-AIR samples suggest that changes occur in the Fe−O local environment upon heating, with the structure becoming more consistent with that of $\gamma$-$Fe_2O_3$.

In contrast, FeO*x* aerogels heated in a low partial pressures of $O_2$ (argon flow) readily convert to distinct nanocrystalline spinel forms, as indicated by X-ray diffraction and HR-TEM. Raman analysis confirms the presence of $Fe_3O_4$ and defects consistent with a $\gamma$-$Fe_2O_3$ structure. The importance of maintaining a low partial pressure of $O_2$ in the contacting gas suggests that Fe(II) sites promote crystallization. Ferrous sites may be present in the as-prepared aerogel and preserved under heating in argon, or they may be generated from Fe(III) sites during the thermal processing by deoxygenation or even by reaction with adsorbed byproducts of the sol−gel synthesis. Tronc et al. examined the effects of Fe(II) ions on the synthesis of various FeO*x* precipitates, demonstrating that the formation of spinel structures was promoted by Fe(II) ions under certain conditions, e.g., for iron oxides with high levels of hydration.[76] This phenomenon was in part attributed to a solid-state reaction whereby structural ordering is driven by electron hopping between Fe(II) and Fe(III) sites, which is further facilitated when the initial iron oxide exists in a hydrated, disordered state. This mechanism would also seem to be plausible for the nanoscale iron oxides described here, but further investigation will be required to confirm this hypothesis.

The aerogel forms of iron oxide described here provide an added property — the nature of their pore−solid architectures — to track as a function of the transformations of the various iron oxide phases. The porosimetry data demonstrate that the extent of temperature/atmosphere-induced crystallinity in the iron oxide solid network correlates well with collapse of the initial pore structure. The disordered as-prepared and poorly crystalline air-treated samples have the largest pores and cumulative pore volume and the widest distribution of pore sizes. The transformation from the as-prepared to the 260-AIR aerogel also results in only modest changes to the pore structure.

In contrast, argon-heated FeO*x* aerogels exhibit an almost total loss in pore volume for pores > 60 nm relative to the as-prepared aerogel, which correlates with the transformation of the amorphous FeO*x* to the nanocrystalline $Fe_3O_4$-$\gamma$-$Fe_2O_3$ form. Even with the pore collapse that accompanies the crystallization process, these nanocrystalline aerogels still retain significant porosity. For example, a porosity of 73% is calculated for the 260-ARG aerogel on the basis of the envelope density (1.5 g $cm^{-3}$) and skeletal density (4.1 g $cm^{-3}$). As the argon-heated samples are progressively heated to higher temperatures, further collapse, densification, and rearrangement of the pore structure occur, along with the formation of larger FeO*x* crystallites within the aerogel architecture (see Table 1).

**Phase Interconversion of Nanocrystalline $Fe_3O_4$ and $\gamma$-$Fe_2O_3$.** Due to the structural similarities of maghemite and magnetite, these phases can typically be interconverted with

(76) Tronc, E.; Belleville, P.; Jolivet, J. P.; Livage, J. *Langmuir* **1992**, *8*, 313−319.

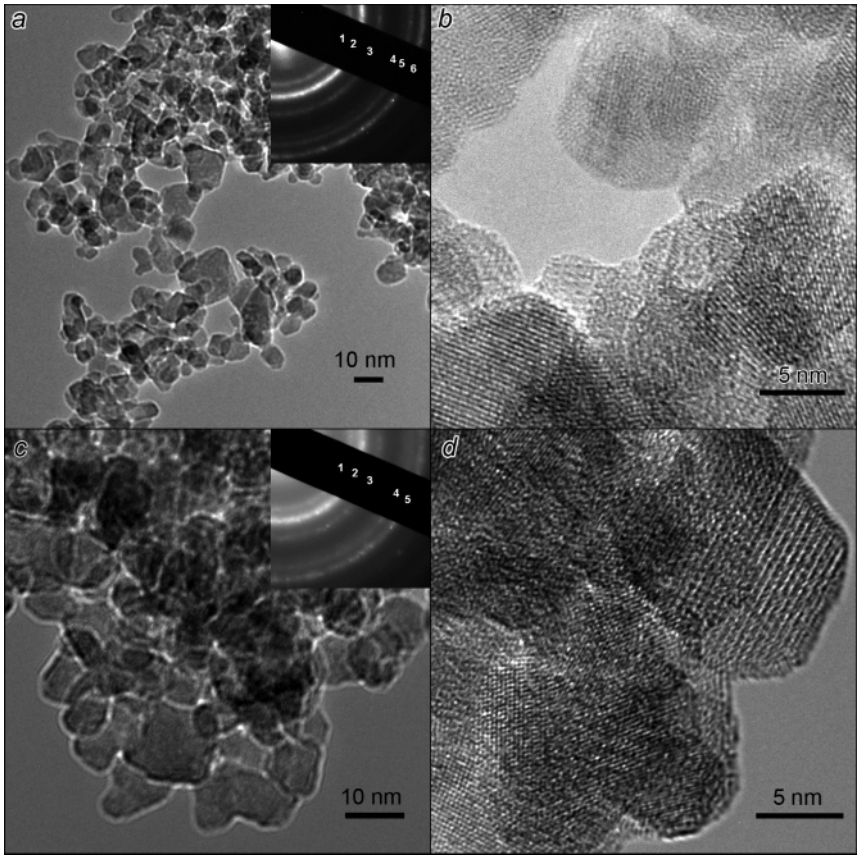


***Figure 6.*** Transmission electron microscopy of the 260-ARG-AIR (a,b) and 260-ARG-AIR-ARG (c,d) samples. The labels on the diffraction patterns in the insets to (a) and (c) correspond to (1) (*220*), (2) (*311*), (3) (*400*), (4) (*422*), (5) (*511*), and (6) (*440*) spacings of the $Fe_3O_4$ and $\gamma$-$Fe_2O_3$ spinel-type cubic structures.

thermal treatments in the presence of controlled partial pressures of oxygen. We observe this same phenomenon with these nanocrystalline FeO*x* aerogels. Beginning with the well-crystallized 260-ARG aerogel, we used subsequent thermal processing under either inert or oxidizing atmospheres in an attempt to tune the phase of the aerogel between $Fe_3O_4$ and $\gamma$-$Fe_2O_3$. Thermal treatment in air at 260 °C converts the blue-black 260-ARG aerogel, previously identified as containing a significant $Fe_3O_4$ component, to a red-orange color. This sample, 260-ARG-AIR, exhibits a surface area (132 $m^2\ g^{-1}$) and cumulative pore volume (0.946 $cm^3\ g^{-1}$) that are only slightly diminished relative to the initial sample, 260-ARG (143 $m^2\ g^{-1}$ and 1.04 $cm^3\ g^{-1}$).

When sample 260-ARG-AIR is reheated at 260 °C in argon to form sample 260-ARG-AIR-ARG, a reddish-black solid results, with somewhat nonuniform coloration. The surface areas and pore volumes of samples 260-ARG-AIR and 260-ARG-AIR-ARG are only modestly reduced with these subsequent thermal treatments, and their PSD plots are also largely unchanged relative to the 260-ARG aerogel (Figure 1d). A comparison of this series of samples by X-ray diffraction shows only subtle shifts in the spinel diffraction pattern that are difficult to assign to a particular phase ($Fe_3O_4$ vs $\gamma$-$Fe_2O_3$).

Electron microscopy studies indicate that these further heat treatments produce a very modest increase in particle size, from an average of 7 nm for 260-ARG to 8.5 nm for both 260-ARG-AIR and 260-ARG-AIR-ARG, but do not cause major changes in the long-range crystal structure. Figure 6 compares the morphology, electron diffraction, and lattice images of the 260-ARG-AIR and 260-ARG-AIR-ARG aerogels. The electron diffraction is sharper and the lattice fringes are more well-ordered for the 260-ARG-AIR aerogel than for the 260-ARG-AIR-ARG sample. Just as for the 260-ARG aerogel, the electron diffraction patterns of these samples index to either $Fe_3O_4$ or $\gamma$-$Fe_2O_3$, in agreement with the X-ray diffraction data. Some evidence for local tetragonal distortions in the lattice images of 260-ARG-AIR is also observed.

The phase transformation of $Fe_3O_4$ to a defect spinel with a phase similar to $\gamma$-$Fe_2O_3$ has been shown to induce changes in the infrared spectra.[77] Heating the 260-ARG aerogel in air to form 260-ARG-AIR decreases the Raman relative intensity $A_{667}/A_{tot}$ from 0.73 to 0.49, which is highly consistent with the $\gamma$-$Fe_2O_3$ phase (see Figure 7). Heating the $\gamma$-$Fe_2O_3$-like 260-ARG-AIR aerogel in argon to form 260-ARG-AIR-ARG increases $A_{667}/A_{tot}$ to 0.70, recovering a local structure that is more characteristic of $Fe_3O_4$, but not completely reversed to the initial 260-ARG aerogel form ($A_{667}/A_{tot} = 0.73$). This analysis confirms that thermal treatments under controlled atmospheres can be used to tune the vacancy content of the spinel structure within certain limits.

The ability to toggle the $Fe_3O_4/\gamma$-$Fe_2O_3$ content via the generation/removal of vacancies with simple thermal treatments greatly extends the versatility of these iron oxide nanoarchitectures in terms of their physical and chemical properties. For example, although direct heating in air does not produce a well-crystallized $\gamma$-$Fe_2O_3$ aerogel, the sequence of an initial argon

(77) Nasrazadani, S.; Raman, A. *Corros. Sci.* **1993**, *34*, 1355−1365.

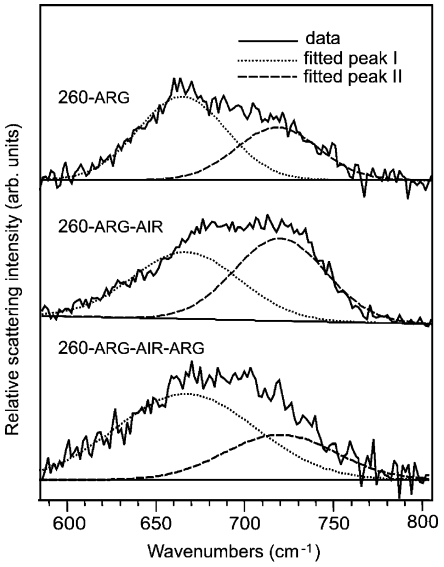


***Figure 7.*** Raman spectra of FeO*x* aerogel samples 260-ARG, 260-ARG-AIR, and 260-ARG-AIR-ARG in the 585−805 $cm^{-1}$ region. The spectra were deconvolved into a band at 665−667 $cm^{-1}$ (peak I) and a band at 720−725 $cm^{-1}$ (peak II) by curve-fitting analysis.

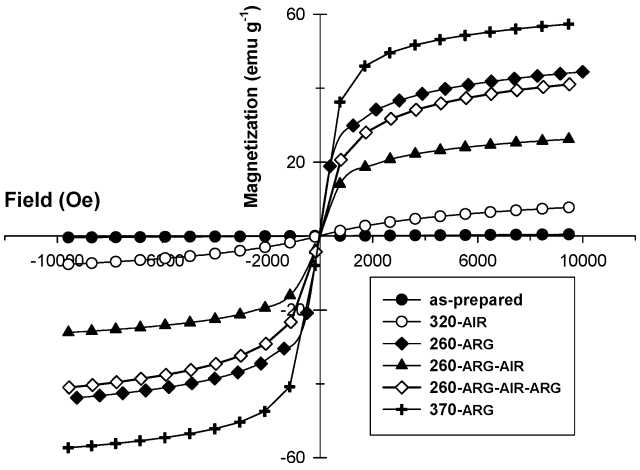


***Figure 8.*** Vibrating sample magnetometry measurements for FeO*x* aerogel powders with various thermal treatments. Measurements were performed at ambient temperature.

treatment followed by air oxidation does yield a nanocrystalline aerogel that is predominantly $\gamma$-$Fe_2O_3$. da Costa et al. reported a related series of observations for sol−gel-derived iron oxide precipitates.[78]

**Magnetic Characterization.** The magnetic properties of the various FeO*x* aerogels corroborate the trends observed by the other characterization methods. The initial magnetization vs field measurements of the FeO*x* aerogels were performed using VSM operating at ambient temperatures, with the field sweeping from −10 to 10 kOe (see Figure 8). As expected, the amorphous, as-prepared FeO*x* aerogel behaves as a weak paramagnet displaying no saturation or coercivity. The poorly crystallized aerogels prepared by direct calcination in air (samples 260-AIR and 320-AIR) are only weakly paramagnetic. The FeO*x* aerogels processed under argon atmosphere exhibit magnetic behavior characteristic of a superparamagnetic material, with a large

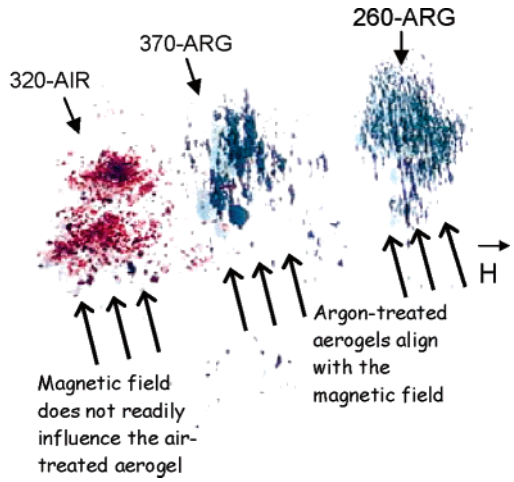


***Figure 9.*** FeO*x* aerogels (as powders) in the presence of a laboratory magnet (magnetic base for rod-mounted components).

saturation magnetization, $\sigma_s$, and no hysteresis at room temperature. The values of $\sigma_s$ for these samples (see Table 1) are lower at ambient conditions relative to bulk forms of $Fe_3O_4$ ($\sigma_s$ = 92 emu $g^{-1}$) and $\gamma$-$Fe_2O_3$ ($\sigma_s$ = 74 emu $g^{-1}$), which is a phenomenon that has been ascribed to the presence of magnetically inactive layers at nanoparticle surfaces.[79] This effect becomes more pronounced as particle size decreases. In these FeO*x* nanoarchitectures, the treatment temperature largely determines the FeO*x* particle size. Thus, sample 370-ARG, with a particle size of ~18.5 nm, exhibits a higher $\sigma_s$ (57 emu $g^{-1}$) than sample 260-ARG, with ~7-nm crystallites and a $\sigma_s$ of 44 emu $g^{-1}$.

A qualitative ranking of the magnetic susceptibility of these materials is readily seen by eye in a simple laboratory experiment with a hand-held magnet, as shown in Figure 9. The greatest alignment of the powdered form of the aerogel occurs for the 370-ARG material, which exhibited the highest magnetization, while negligible alignment appears to occur for 320-AIR.

For iron oxides with similar particle sizes and surface areas, the saturation magnetization can also be an effective parameter for distinguishing between the $Fe_3O_4$ and $\gamma$-$Fe_2O_3$ phases, where the lower $\sigma_s$ values for $\gamma$-$Fe_2O_3$ relative to $Fe_3O_4$ are attributed to the presence of cation vacancies in the $\gamma$-$Fe_2O_3$ lattice.[80] This same analysis can be applied to the nanocrystalline FeO*x* aerogels presented here, beginning with sample 260-ARG. As shown earlier, this sample can be oxidized in air at 260 °C (forming sample 260-ARG-AIR), with no significant change in particle size, surface area, or pore structure, while converting the local structure to a phase more consistent with $\gamma$-$Fe_2O_3$ according to the Raman spectrum. Upon oxidation, $\sigma_s$ markedly decreases from 44.4 to 26.0 emu $g^{-1}$, which is consistent with the progressive transformation of $Fe_3O_4$ to $\gamma$-$Fe_2O_3$ accompanied by an increase in the vacancy population. This oxidative phase transformation is partially reversed when the 260-ARG-AIR aerogel is reheated, but now in argon to form 260-ARG-AIR-ARG, which exhibits an increased $\sigma_s$ of 41.0 emu $g^{-1}$. The magnetization does not entirely recover to that of the initial 260-ARG aerogel ($\sigma_s$ = 44.1 emu $g^{-1}$), a result which is

(78) da Costa, G. M.; De Grave, E.; de Bakker, P. M. A.; Vandenberghe, R. E. *J. Solid State Chem.* **1994**, *113*, 405−412.
(79) Berkowitz, A. E.; Schuele, W. J.; Flanders, P. J. *J. Appl. Phys.* **1968**, *39*, 1261−1263.
(80) Goss, C. J. *Phys. Chem. Miner.* **1988**, *16*, 164−171.

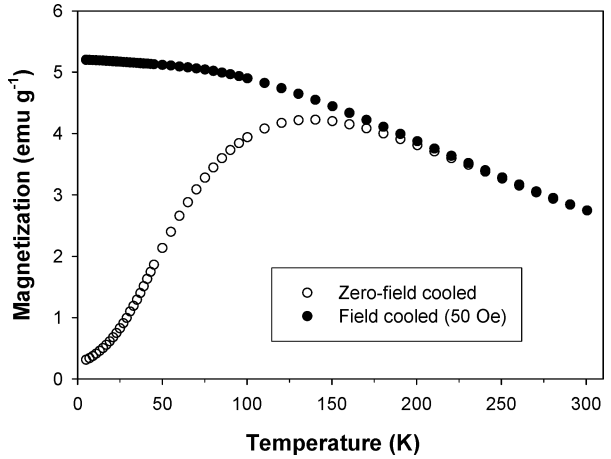


***Figure 10.*** SQUID measurements on sample 260-ARG-AIR-ARG. Measurements were performed at 50 Oe with temperature scanned from 5 to 300 K.

highly consistent with the Raman analysis of these materials, which showed that the 260-ARG-AIR-ARG aerogel retained a slightly higher vacancy content than the 260-ARG aerogel.

The SQUID characterization of the nanocrystalline FeO*x* aerogels confirms their superparamagnetism; a typical magnetization vs temperature plot is presented in Figure 10, in this particular case for the 260-ARG-AIR-ARG aerogel. As the sample is cooled in zero applied field, the magnetic spins of the sample are frozen in an antiparallel alignment. Once a field is applied and the temperature is increased, the spins start to align, increasing the magnetization to a maximum at the blocking temperature, $T_B$, where thermal fluctuations randomize the spins. When the sample is cooled in the applied magnetic field, the spins are frozen in a parallel fashion. The magnetization remains relatively unchanged until the blocking temperature (see $T_B$ values in Table 1). As the temperature is increased, the field-cooled (FC) and zero-field-cooled (ZFC) curves merge. The blocking temperature for each particular sample depends on the field strength as well as the measurement technique. This behavior can be best explained by superparamagnetism.[81−83] In a future publication, we will present a more detailed analysis of the magnetic properties of these aerogels, focusing on such issues as the magnetic domain size and how the individual iron oxide nanoparticles that comprise the solid component of the aerogel nanoarchitecture interact in the presence of magnetic fields.

**Future Opportunities for Nanocrystalline FeO*x* Aerogels.** The magnetic FeO*x* aerogels described here can be achieved with partial control of the pore−solid architecture, the nanocrystalline phase, the nanoparticle size, and the resulting magnetic properties. We have also recently extended this sol−gel approach to produce nanocrystalline Mn−FeO*x* aerogels with the $MnFe_2O_4$ spinel phase, which exhibit related magnetic properties and morphologies.[84] Both the FeO*x* and Mn−FeO*x* aerogels generated with this synthetic approach provide the added benefit of a stable monolithic form, whereas previous examples of magnetic ferrite aerogels[85,86] were produced as powders. The magnetic aerogels reported here can also be contrasted with mesoporous iron oxides synthesized by surfactant-templating methods.[23−25] These aerogel forms, while requiring the additional processing step of supercritical $CO_2$ extraction, can be produced with a broad range of pore sizes spanning the mesopore and small macropore size range (10−80 nm), whereas the templated mesoporous iron oxides reported to date have pore sizes restricted to less than 10 nm. The flexibility of the aerogel route with respect to optimizing pore size and structure is a critical advantage for the future application of these materials. With this well-stocked toolbox of variably magnetic aerogels, we can now investigate the interaction of paramagnetic liquid- and gas-phase species within a monolithic, totally magnetized nanoarchitecture, with potential applications in sensing and separations.

Gwak et al. recently described their attempts to separate gaseous mixtures of $O_2$ and $N_2$ on the basis of magnetic interactions within a porous alumina membrane impregnated with magnetic oxide nanoparticles; their initial studies showed only limited selectivity.[87] The aerogels described here may be ideal membranes for such separation schemes, where high magnetic field gradients should be generated at the surfaces of the nanocrystallites within the mesoporous volume of the aerogel when subjected to an external magnetic field. The aperiodic design of these pore−solid architectures may also be advantageous for promoting internal magnetic fields that are more inhomogeneous than would be observed for an ordered porous structure. In the case of magnetic applications, the particular phase mixture of these aerogels ($Fe_3O_4$-rich vs $\gamma$-$Fe_2O_3$-rich) will be of less concern, as both are superparamagnetic, whereas long-term chemical stability may be a more important consideration.

The nature of the nanocrystalline phase and degree of crystallinity for the FeO*x* aerogel will be more critical for catalytic applications and for electrochemical performance, particularly when used as Li ion insertion electrodes. Swider-Lyons et al. previously demonstrated that thermal treatments that promote cation vacancy formation in polycrystalline $V_2O_5$ improved the Li ion storage capacity.[88] As the $\gamma$-$Fe_2O_3$ spinel is produced with formation of cation vacancies for charge balance, such nanocrystalline forms, combined with the advantageous architecture of the aerogel,[22] should yield moderate-voltage electrode structures with useful characteristics for energy storage. Preliminary investigations of the electrochemical performance of the FeO*x* nanoarchitectures presented in this report are currently underway.

## Conclusions

Using epoxide-based sol−gel methods and subsequent thermal processing steps, we have produced nanocrystalline iron oxide architectures that retain the significant porosities and surface areas expected from an aerogel, while also exhibiting

(81) Dormann, J. L.; Viart, N.; Rehspringer, J. L.; Ezzir, A.; Niznansky, D. *Hyp. Interact.* **1998**, *112*, 89−92.
(82) Dormann, J. L., Fiorani, D., Eds. *Magnetic Properties of Fine Particles*; North-Holland: Rome, Italy, 1991.
(83) Dormann, J. L.; Fiorani, D.; Cherkaoui, R.; Tronc, E.; Lucari, F.; D'Orazio, F.; Spinu, L.; Nogues, M.; Kachkachi, H.; Jolivet, J. P. *J. Magn. Magn. Mater.* **1999**, *203*, 23−27.
(84) Long, J. W.; Logan, M. S.; Carpenter, E. E.; Rolison, D. R. *J. Non-Cryst. Solids* **2004**, in press.
(85) Hamdeh, H. H.; Barghout, K.; Ho, J. C.; Willey, R. J.; O'Shea, M. J.; Chaudhuri, J. *J. Magn. Magn. Mater.* **2000**, *212*, 112−120.
(86) Hamdeh, H. H.; Ho, J. C.; Oliver, S. A.; Willey, R. J.; Oliveri, G.; Busca, G. *J. Appl. Phys.* **1997**, *81*, 1851−1857.
(87) Gwak, J. H.; Ayral, A.; Rouessac, V.; Cot, L.; Grenier, J. C.; Choy, J. H. *Microporous Mesoporous Mater.* **2003**, *63*, 177−184.
(88) Swider-Lyons, K. E.; Love, C. T.; Rolison, D. R. *Solid State Ionics* **2002**, *152−153*, 99−104.

superparamagnetic properties. The iron oxidation state and related vacancy content of these spinel $Fe_3O_4$-$\gamma$-$Fe_2O_3$ phases can be easily tuned while also preserving the nanoscale particle size and pore structure of the aerogel. With effective control of the pore−solid architecture, the nanocrystalline phase, and subsequent magnetic properties, we can now design porous, magnetic nanoarchitectures for a wide range of future applications.

**Acknowledgment.** Financial support for this work was provided by the Defense Advanced Research Projects Agency and the Office of Naval Research.

**Supporting Information Available:** Results of X-ray photoelectron spectroscopy analyses. This material is available free of charge via the Internet at http://pubs.acs.org.

JA046044F